

## Comparison of embedded atom method potentials for small aluminium cluster simulations

This article has been downloaded from IOPscience. Please scroll down to see the full text article.

2009 J. Phys.: Condens. Matter 21 144206

(<http://iopscience.iop.org/0953-8984/21/14/144206>)

View [the table of contents for this issue](#), or go to the [journal homepage](#) for more

Download details:

IP Address: 129.252.86.83

The article was downloaded on 29/05/2010 at 18:55

Please note that [terms and conditions apply](#).

# Comparison of embedded atom method potentials for small aluminium cluster simulations

Akin Budi<sup>1</sup>, David J Henry<sup>1</sup>, Julian D Gale<sup>2</sup> and Irene Yarovsky<sup>1,3</sup>

<sup>1</sup> Applied Physics, School of Applied Sciences, RMIT University, GPO Box 2476V, Melbourne, VIC 3001, Australia

<sup>2</sup> Nanochemistry Research Institute, Department of Applied Chemistry, Curtin University of Technology, GPO Box U1987, Perth, WA 6845, Australia

E-mail: [irene.yarovsky@rmit.edu.au](mailto:irene.yarovsky@rmit.edu.au)

Received 4 September 2008, in final form 9 October 2008

Published 18 March 2009

Online at [stacks.iop.org/JPhysCM/21/144206](http://stacks.iop.org/JPhysCM/21/144206)

## Abstract

In this paper, we present a comparison of the performance of a series of embedded atom method potentials for the evaluation of bulk and small aluminium cluster geometries and relative energies, against benchmark density functional theory calculations. In general, the non-pairwise potential-B (NP-B), which was parametrized against Al cluster data, performs the best.

(Some figures in this article are in colour only in the electronic version)

## 1. Introduction

Light-metal hydrides have for some time been considered for hydrogen storage application due to their high hydrogen content [1, 2]. For example, aluminium–lithium-based metal hydrides can store up to 10.6 wt% hydrogen and magnesium-based metal hydrides can store up to 7.6 wt% hydrogen [3]. Despite this high storage capacity, none of the materials so far have exhibited fast enough kinetics for hydrogen adsorption/desorption, which is essential for practical applications. In addition, there remain uncertainties about the thermal behaviour of crystal structures, atomic configurations, and electronic structures for various intermediate phases [3]. Therefore, a significant amount of research is currently focused on temperature effects and enhancing the kinetics by developing catalysts that eliminate the need for the high temperature/pressure conditions currently required for the rehydriding/dehydriding cycle [3–5].

Clusters and other nanostructures are known to have different properties to bulk materials and may provide a good alternative as a novel medium with high hydrogen storage capacity and good kinetics. Aluminium clusters have recently attracted attention from both cluster and hydrogen storage research groups [6, 7]. We have previously used density functional theory (DFT) techniques implemented in

DMol<sup>3</sup> [8, 9] to study the interactions of bare and doped (Mg, Si) aluminium clusters with hydrogen [7, 10] and identified a cluster (Al<sub>12</sub>H<sub>20</sub>) with a high hydrogen storage capacity [11]. Furthermore, we recently discovered that while there is a modest barrier for chemisorption of H<sub>2</sub> on a single Al<sub>12</sub>Mg, H<sub>2</sub> was found to spontaneously dissociate between two closely spaced Al<sub>12</sub>Mg clusters [12], suggesting that doped Al clusters can be used as building blocks for a potential hydrogen storage material.

Aluminium clusters are also of interest to hydrogen storage research due to their potential to form alanes and alanates [13, 14]. Balde *et al* have recently demonstrated that large clusters of NaAlH<sub>4</sub> (with a diameters of 2–10 Å) have the potential for hydrogen storage of 2 wt% capacity with faster kinetics than the bulk material (desorption temperature lower than 343 K) [15]. Zidan *et al* have studied titanium/zirconium-doped NaAlH<sub>4</sub> compounds using thermal-programmed desorption. The study indicated that the NaAlH<sub>4</sub> compounds have a hydrogen storage capacity of 4.0 wt% with fast kinetics (dehydriding temperature of 398 K) [5]. While the hydrogen capacity is less than the current US department of energy (DOE) goal of 6.0 wt% by 2010 and 9.0 wt% by 2015 [16], it demonstrates the potential of alanates as candidate hydrogen storage materials.

Although the ideal approach to the study of metal clusters involves the use of quantum mechanically based

<sup>3</sup> Author to whom any correspondence should be addressed.

methods, theoretical studies of clusters beyond  $\sim 100$  atoms rapidly become computationally less tractable with DFT, especially when the structural complexity is taken into account. Therefore, less accurate but more practical methods must be used to overcome these limitations. In this paper, we test the embedded atom method (EAM) potentials for small aluminium clusters against existing experimental and theoretical data in order to explore the possibility of employing EAM potentials to model larger clusters, cluster assemblies, and nanocrystals, that are currently demanding for study by DFT. Furthermore, having established which potential(s) performs the best for bare aluminium clusters, we plan to extend the potential to include interaction parameters for other metals (e.g. Mg, Si, Li, Na) where necessary, as well as hydrogen, to enable hydrogen adsorption on cluster-assembled light-metal nanomaterials to be studied.

The embedded atom method (EAM) was originally developed by Daw and Baskes in order to study hydrogen embrittlement in nickel [17] and has since been used extensively to study metallic systems [18]. An extension of this method is also available in the form of modified EAM (MEAM) [19–21]. The inclusion of angular dependent terms in MEAM allows it to describe the liquid structure, stacking faults, and surface energies quite accurately even when it is short-ranged [19, 20]. Baskes noted that while EAM is sufficient to describe FCC structures, MEAM affords better description of BCC structures and is a necessity to describe diamond cubic structures [19]. While there are currently many available EAM potentials for specific systems consisting of one or more elements, including aluminium, most of these potentials have been constructed by fitting to bulk structures [22–26]. It has been demonstrated that the Sutton–Chen, Cleri–Rosato, and Streitz–Mintmire potentials, all parametrized for aluminium, perform very well for structural features and thermodynamic behaviour of bulk materials and sufficiently large structures [23–25]. While Truhlar and co-workers have previously demonstrated the limitations of bulk-fitted EAM potentials for the accurate determination of cluster energies, no discussion was provided on the ability of these potentials for cluster structure prediction. Nevertheless, Truhlar and co-workers have parametrized the Mei–Davenport EAM potential [27] using accurately determined characteristics of a library of small aluminium clusters ( $\text{Al}_2$ – $\text{Al}_{177}$ ) and bulk aluminium obtained by first principles methods [28, 29]. In this work, we present a comparison of the structural and thermodynamical behaviour of a number of clusters of interest to our longer term research goals modelled using the Truhlar potential (NP-B) and three commonly used bulk-fitted EAM potentials [23–25]. We explore the ability of the potentials to accurately predict equilibrium cluster geometries, to identify local minima and relative energies of clusters against our previously tested benchmark PBE/DNP level. We also present preliminary results of cluster melting behaviour evaluated using each of the potentials.

## 2. Methods

### 2.1. EAM potentials

The EAM potentials chosen for this study were the Sutton–Chen [25], Cleri–Rosato, [23], Streitz–Mintmire [24], and NP-B [28]. The functional form and parameters of the EAM potentials used in this work are summarized in table 1.

The charge of each aluminium atom for all the above potentials is zero, including the Streitz–Mintmire potential, because we are interested in purely metallic systems. For each of the functional forms considered, the pair potential and many-body cut-off is 12.0 Å, except for Streitz–Mintmire where the latter is 8.0 Å.

The EAM functional of the NP-B potential is given in the following Mei–Davenport form [27, 30];

$$F_i(\bar{\rho}_i) = \sum_i -E_c \left[ 1 - \frac{\alpha}{\beta} \ln \left( \frac{\bar{\rho}_i}{\rho_e} \right) \right] \left( \frac{\bar{\rho}_i}{\rho_e} \right)^{\frac{\alpha}{\beta}} + \sum_{m=1}^3 \frac{1}{2} \phi_0 s_m \exp[-(\sqrt{m}-1)\gamma] \times \left[ 1 + (\sqrt{m}-1)\delta - \frac{\sqrt{m}\delta}{\beta} \ln \left( \frac{\bar{\rho}_i}{\rho_e} \right) \right] \left( \frac{\bar{\rho}_i}{\rho_e} \right)^{\frac{\sqrt{m}\gamma}{\beta}},$$

with the following parameters:  $E_c = 2.834$  eV;  $\alpha = 4.954$ ;  $\beta = 5.203$ ;  $\gamma = 5.824$ ;  $\delta = 8.969$ ;  $\phi_0 = 0.2095$  eV;  $s_1 = 6.928$ ;  $s_2 = 3.861$ ; and  $s_3 = 15.50$ . The parameter  $\rho_e$  is an adjustable parameter determined from fitting the calculated electron density [30]. The density term is given by the equation;

$$\bar{\rho}_i = \rho_e \sum_i \sum_{l=0}^5 \frac{c_l}{12} \left( \frac{r_i}{r_0} \right)^l,$$

with the following parameters:  $c_0 = 0.4333$ ;  $c_1 = -7.305$ ;  $c_2 = 29.812$ ;  $c_3 = -54.44$ ;  $c_4 = 48.41$ ;  $c_5 = -15.50$ ; and  $r_0 = 2.760$  Å. The parameter  $\rho_e$  in the density term cancels exactly in the EAM functional.

Finally, the pair potential is given in the following form;

$$\phi_{ij}(r_{ij}) = -\phi_0 \left[ 1 + \delta \left( \frac{r}{r_0} - 1 \right) \right] \exp \left[ -\gamma \left( \frac{r}{r_0} - 1 \right) \right],$$

with the following parameters:  $\phi_0 = 0.2095$  eV;  $\delta = 8.969$ ;  $\gamma = 5.824$ ; and  $r_0 = 2.760$  Å.

The density and pair potential terms are multiplied by a taper function as follows;

$$\bar{\rho}_{i,\text{taper}}(r) = \bar{\rho}_i(r) f_{\text{taper}}(r)$$

$$\phi_{ij,\text{taper}}(r) = \phi_{ij}(r) f_{\text{taper}}(r),$$

where

$$f_{\text{taper}}(r) = \begin{cases} 0 & r \geq r_{\text{cut}} \\ (1-x)^3(1+3x+6x^2) & r_m \leq r < r_{\text{cut}} \\ 1 & r < r_m, \end{cases}$$

and  $x = \frac{(r-r_m)}{r_{\text{cut}}-r_m}.$

**Table 1.** Functional form and parameters for the bulk-fitted EAM potentials.

Potential	EAM functional	EAM density	Pair potential
Sutton–Chen	$F_i(\bar{\rho}_i) = -\sum_i A_i \sqrt{\bar{\rho}_i}$ $A = 1.000 \text{ eV}$	$\bar{\rho}_i = \sum_i C r_{ij}^{-6}$ $C = 1303.927 1480 \text{ \AA}^6$	$\phi_{ij}(r_{ij}) = \frac{A}{r^7}$ $A = 592.419 5621 \text{ eV \AA}^7$
Clari–Rosato	$F_i(\bar{\rho}_i) = -\sum_i A_i \sqrt{\bar{\rho}_i}$ $A = 1.000 \text{ eV}$	$\bar{\rho}_i = \sum_i A \exp[-B(r_{ij} - r_0)]$ $A = 1.731 856$ $B = 1.757 117 \text{ \AA}^{-1}$ $r_0 = 2.863 782 \text{ \AA}$	$\phi_{ij}(r_{ij}) = A \exp(-\frac{r}{\rho})$ $A = 1342.424 092 \text{ eV}$ $\rho = 0.332 534 \text{ \AA}$
Streitz–Mintmire	$F_i(\bar{\rho}_i) = -\sum_i A_i \sqrt{\bar{\rho}_i}$  $A = 1.987 699 \text{ eV}$	$\bar{\rho}_i = \sum_i A \exp[-B(r_{ij} - r_0)]$  $A = 0.147 699 \text{ eV}$ $B = 2.017 519 \text{ \AA}^{-1}$ $r_0 = 3.365 875 \text{ \AA}$	$\phi_{ij}(r_{ij}) = A \exp(-\frac{r}{\rho})$ $-B[1 + C(\frac{r}{r_0} - 1)] \exp[-C(\frac{r}{r_0} - 1)]$ $A = 4.474 755 \text{ eV}$ $B = 0.159 472 \text{ eV}$ $C = 5.949 1436 72$ $\rho = 0.991 317 \text{ \AA}$ $r_0 = 3.365 875 \text{ \AA}$

The  $r_m$  parameter is the distance for the start of the tapering function, which is set to 4.83 Å, and  $r_{\text{cut}}$  is the cut-off for both the many-body potential and the pair potential, which is set to 5.382 Å. Similarly to the other potentials studied here, the charge of each aluminium atom is zero. The graphical representation of each of the terms of the potentials is shown in table 2.

## 2.2. Computational procedure

In order to compare the EAM potentials, we have calculated the structural properties of Al<sub>2</sub>, Al<sub>3</sub>, Al<sub>12</sub>, Al<sub>13</sub>, and bulk aluminium using the GULP simulation package [31] where all the potentials described above have been implemented. In addition, we have also calculated the melting temperatures for the larger clusters of Al<sub>34</sub> and Al<sub>55</sub>. Bulk Al was constructed as a face-centred cubic lattice with lattice constant of 4.050 Å. Constant pressure geometry optimization was then performed for the bulk system. Geometry optimization was conducted for Al<sub>2</sub>, Al<sub>12</sub>, and Al<sub>13</sub> clusters using the EAM potentials and compared with the optimized structures obtained by DFT calculations, which provide a benchmark for this study. We calculated the binding energy curves for Al<sub>2</sub> to assess the accuracy of the potentials in predicting the equilibrium bond separation as well as to compare the overall shape of the curves. In order to assess the angular dependence of the potentials, we calculated the binding energy curves for different structural configurations of Al<sub>3</sub> with arbitrary Al–Al bond lengths ( $r_1, r_2 = 2, 2.3, 2.506, 2.863, 3.5, \text{ and } 5 \text{ \AA}$ ). For the Al<sub>12</sub> and Al<sub>13</sub> clusters, we have also calculated the EAM single point energies for a range of DFT optimized structural isomers in order to assess the ability of each potential to predict the relative stability.

For the EAM-based methods, geometry optimization was performed using the Broyden–Fletcher–Goldfarb–Shanno (BFGS) minimizer [32] until the forces fell below 0.1 eV Å<sup>-1</sup>, after which the rational functional optimization (RFO) method [33] was used in order to ensure the positive definite nature of the Hessian matrix. The convergence criteria applied were 10<sup>-5</sup> eV for energy, 10<sup>-3</sup> eV Å<sup>-1</sup> for force (with

individual force components not exceeding 10<sup>-2</sup> eV Å<sup>-1</sup>), and displacements not exceeding 10<sup>-5</sup> Å. For the evaluation of the melting temperature, molecular dynamics (MD) calculations were performed at temperatures between 150 and 800 K. For each temperature, the MD calculations were performed for 1 ns with a timestep of 0.5 fs. Each calculation starts with a temperature of 100 K and applying a temperature ramp of 0.2 K fs<sup>-1</sup>.

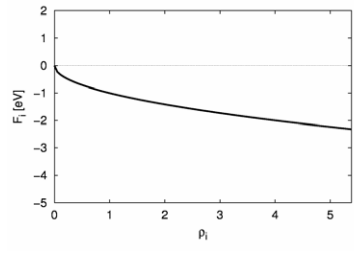
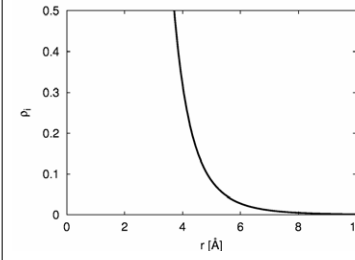
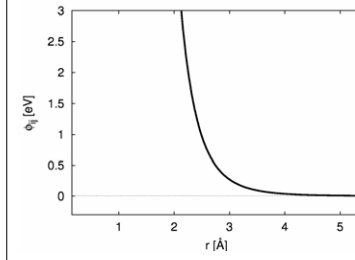
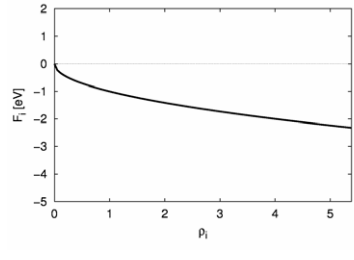
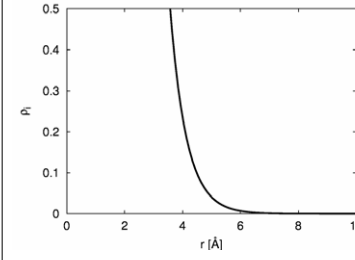
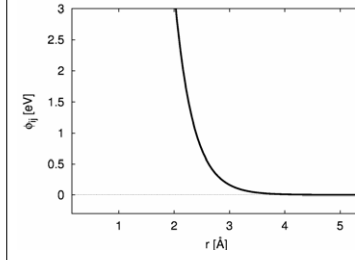
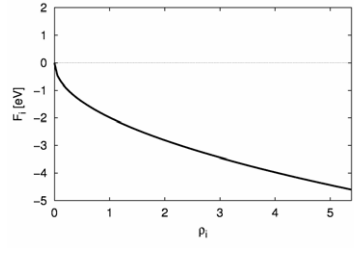
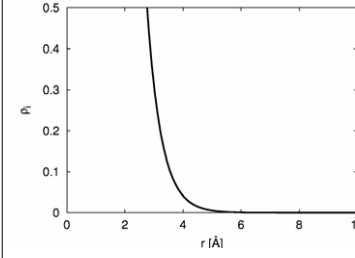
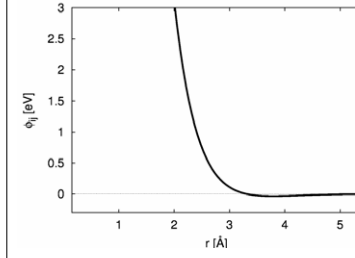
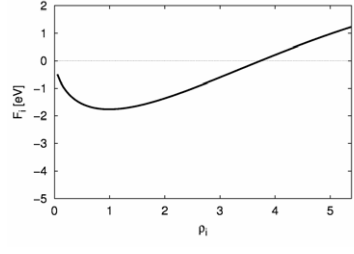
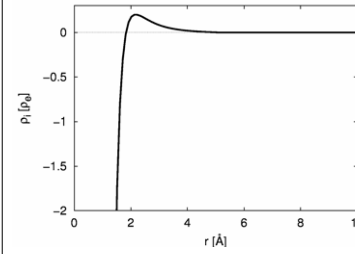
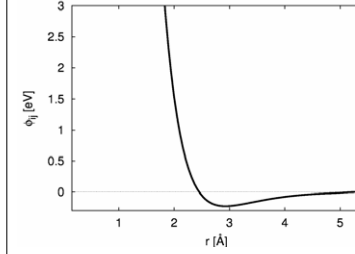
DFT calculations were performed using DMol<sup>3</sup> [8, 9] with the Perdew–Burke–Ernzerhof (PBE) functional [34, 35] and a double numerical polarized (DNP) basis set, giving a proper description of Al atoms [36]. This method has been well validated in previous studies on Al clusters [7, 10, 11]. Thermal occupation with an energy of 0.136 eV was utilized to improve convergence. An orbital cut-off of 10.0 Å has been used throughout this study. The criteria of convergence used for the geometry optimization procedure were 2.721 × 10<sup>-4</sup> eV for energy, 5.442 × 10<sup>-2</sup> eV Å<sup>-1</sup> for force, and 0.005 Å for displacement.

## 3. Results and discussion

### 3.1. Bulk properties

We begin our assessment with a review of the performance of each potential for the determination of bulk Al properties. Table 3 summarizes the bulk properties of aluminium predicted by the different potentials. Although most of the presented values are obtained from the literature, we have independently determined these properties using each of the potentials to ensure accurate implementation of the potentials in GULP. The values calculated in this work and not reported in the original studies are denoted by the hash (#) symbol. The bulk and shear moduli that were not given in the literature have been derived from the elastic constants and are denoted by the star (\*) symbol. As can be seen from the table, all EAM potentials perform well for determining the structural parameters of bulk aluminium showing close agreement with experimental lattice constant and density. Furthermore, all potentials give a binding energy per atom to within 2% of the

**Table 2.** The graphical representation of each of the terms of the potentials used in the present work. Note that the EAM density of the NP-B potential is expressed in terms of the parameter  $\rho_e$ .

Potential	EAM functional	EAM density	Pair potential
Sutton-Chen			
Cleri-Rosato			
Streitz-Mintmire			
NP-B			

experimental value and density to within 1%. Interestingly, the NP-B potential performed equally well as compared to the bulk-fitted potentials for the structural and energetic properties, because the training set included a range of cluster sizes as well as the bulk with different weightings [28]. However, while the Cleri–Rosato and Streitz–Mintmire potentials showed good agreement with the experimental elastic constants, the Sutton–Chen and NP-B showed significantly larger variations. Not surprisingly, the better performance of Cleri–Rosato and Streitz–Mintmire potentials in this regard can be attributed to the fact that the elastic constants were included in the fitting procedure for these potentials, while this is not the case for Sutton–Chen and NP-B. Nevertheless, the Sutton–Chen potential provides a reasonable estimate of the bulk modulus, which can be attributed to the fact that the values for the exponents of density and pair potential were specifically chosen to provide the best approximation to the experimental value of this quantity [25]. The NP-B potential severely overestimates the stiffness of the material, which suggests

its inadequacy in describing bulk materials and surfaces. However, it should be noted that the NP-B potential was developed specifically for clusters and not bulk materials and cannot therefore be expected to predict bulk properties with the same accuracy as the potentials that were developed specifically for this purpose.

### 3.2. $Al_2$ equilibrium separation

Next we focus our attention on the performance of the potentials for the description of the  $Al_2$  dimer. The characterization of  $Al_2$  dimer has provided a challenge for both theory and experiment due to the closeness in energy of the singlet and triplet states.

Although the EAM potential cannot distinguish between the singlet and triplet states, it is curious to see which of the potential energy surfaces associated with the two electronic states each parametrization will favour. Figure 1 shows the comparison of binding energy curves of  $Al_2$  for the EAM

**Table 3.** Theoretical and experimental bulk properties of aluminium.

	Sutton–Chen [25]	Cleri–Rosato [23]	Streitz–Mintmire [24]	NP-B [28]	Experiment
Binding energy per atom (eV)	−3.34	−3.339	−3.39	−3.43	−3.34 [37] −3.339 [38] −3.39 [39] −3.43 [40]
Lattice constant (Å)	4.05	4.05	4.05	4.03	4.05 [37, 38, 41] 4.034 [42]
Density (g cm <sup>−3</sup> )	2.694 <sup>#</sup>	2.702 <sup>#</sup>	2.699 <sup>#</sup>	2.727 <sup>#</sup>	2.70 [43]
Bulk modulus (Voigt average) (GPa)	75.3	81	82.7 <sup>*</sup>	169.0 <sup>#</sup>	76.9 [44] 76 [45]
Shear modulus (Voigt average) (GPa)	11.5 <sup>*</sup>	26.4 <sup>*</sup>	23.8 <sup>*</sup>	78.8 <sup>#</sup>	26.1 [46]
Young’s modulus (GPa)	14.1 <sup>#</sup>	29.4 <sup>#</sup>	19.1 <sup>#</sup>	116.0 <sup>#</sup>	70.3 [46]
Poisson’s ratio	0.468 <sup>#</sup>	0.440 <sup>#</sup>	0.461 <sup>#</sup>	0.386 <sup>#</sup>	0.345 [46]
$c_{11}$ (GPa)	82	95	94	225 <sup>#</sup>	107.3 [44] 107 [45, 47]
$c_{12}$ (GPa)	72	74	77	141 <sup>#</sup>	60.9 [44] 61 [45, 47]
$c_{44}$ (GPa)	16	37	34	103 <sup>#</sup>	28.8 [44] 29 [45] 28 [47]

\* Calculated from the elastic constants in the original reference.

# Calculated in this work.

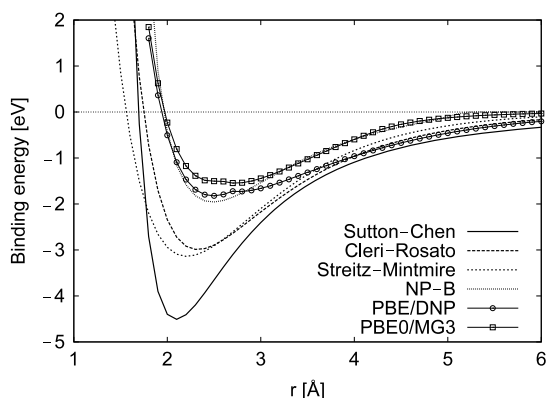


**Figure 1.** Binding energy curve of Al<sub>2</sub> as a function of separation. For the DFT calculations the curve given is that of the lower energy triplet state.

potentials considered in this study, along with the PBE/DNP and PBE0/MG3 levels, the latter of which was used in fitting the NP-B potential [28]. The PBE/DNP binding energy curve compares favourably to the PBE0/MG3 results, with a slightly slower decay of the potential beyond the equilibrium value. The NP-B potential slightly overestimates the depth of the binding energy minimum by 0.412 eV, which is slightly more than the mean unsigned error (MUE) (0.185 eV) reported by Jasper *et al* [28] for the complete Al<sub>2</sub> data set, but agrees well with the long tail behaviour of the PBE0/MG3 results.

The three bulk-fitted EAM potentials significantly overestimate the depth of the binding energy minimum and underestimate the equilibrium separation distance. Jasper *et al* report that the MUE for the Al<sub>2</sub> data set are 1.034, 1.130 eV and 0.776 eV for the Cleri–Rosato, Sutton–Chen and Streitz–Mintmire potentials, respectively [48]. The decay of the binding energy curve for these potentials is also slower

**Table 4.** Al<sub>2</sub> equilibrium separation values. The star (\*) symbol denotes triplet state.

EAM potential	Al <sub>2</sub> equilibrium separation (Å)
Sutton–Chen	2.092
Cleri–Rosato	2.325
Streitz–Mintmire	2.207
NP-B	2.523
PBE/DNP	2.656*
PBE0/MG3	2.730* [49]
CCSD(T, full)/6-311 + G(2df)	2.7157*
Experiment [50]	2.835*

compared to the NP-B potential and indicates a longer range over which the potential acts. The Sutton–Chen potential is observed to have a harder short-range interaction compared to the other potentials and the DFT results. This may indicate its unsuitability for studying small aluminium clusters. The repulsive strength of the Streitz–Mintmire potential is also observed to diminish more rapidly as compared to the other potentials, thus increasing the likelihood of smaller Al–Al separations in a cluster relative to the other potentials.

Table 4 shows the equilibrium separation values for the EAM potentials considered in this study, along with the values obtained by several *ab initio* and DFT calculations, as well as experiment for comparison. The results from the quantum mechanical calculations agree well with the experimental value of 2.835 Å, which corresponds to the low energy X<sup>3</sup>Π<sub>u</sub> state. The Al<sub>2</sub> equilibrium separation distance as calculated using the NP-B potential is 0.133 Å shorter than the value predicted using PBE/DNP, while the bulk-fitted potentials underestimate the equilibrium separation value by an average of 0.45 Å.

This implies that these potentials will result in clusters that are more compact in structure, due to the increased bonding interaction between any two aluminium atoms.

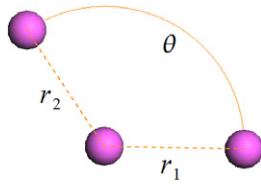


**Figure 2.** Schematic diagram of the Al<sub>3</sub> arrangement.

### 3.3. Al<sub>3</sub>

The next stage of our study involved an investigation of the angular dependence of the binding energy for different structural configurations of Al<sub>3</sub>. Figure 2 provides a schematic representation of the arrangement of Al<sub>3</sub> with definitions of the key variables. Following the methodology of Truhlar and co-workers [28], binding energy curves were obtained for angles ranging from 15° to 175° (in 15° increments) for Al<sub>3</sub> clusters

with arbitrary Al–Al bond lengths ( $r_1, r_2 = 2, 2.3, 2.506, 2.863, 3.5,$  and  $5 \text{ \AA}$ ). We have also included the PBE0/MG3 data that was used to train the NP-B potential [28].

Figure 3 shows the binding energy for the different Al<sub>3</sub> arrangements. All of the bulk-fitted potentials were observed to overestimate the binding energy of the Al<sub>3</sub> cluster. In general, NP-B predicts the binding energy for the selected configurations quite accurately relative to PBE/DNP and PBE0/MG3. For small values of  $r_1$  and  $r_2$ , the EAM potentials were found to be relatively insensitive to the variation in  $\theta$ , for angles greater than equilibrium angular separation (where the binding energy is at its minimum). Except for  $r_1, r_2 = 2.0 \text{ \AA}$ , the Cleri–Rosato and Streitz–Mintmire potentials give almost identical binding energy curves. As the values of  $r_1$  and  $r_2$  were increased, the binding energy minimum was found to occur at successively smaller angles. The electronic state of the trimer at the equilibrium angular separation is  $^2A_1'$

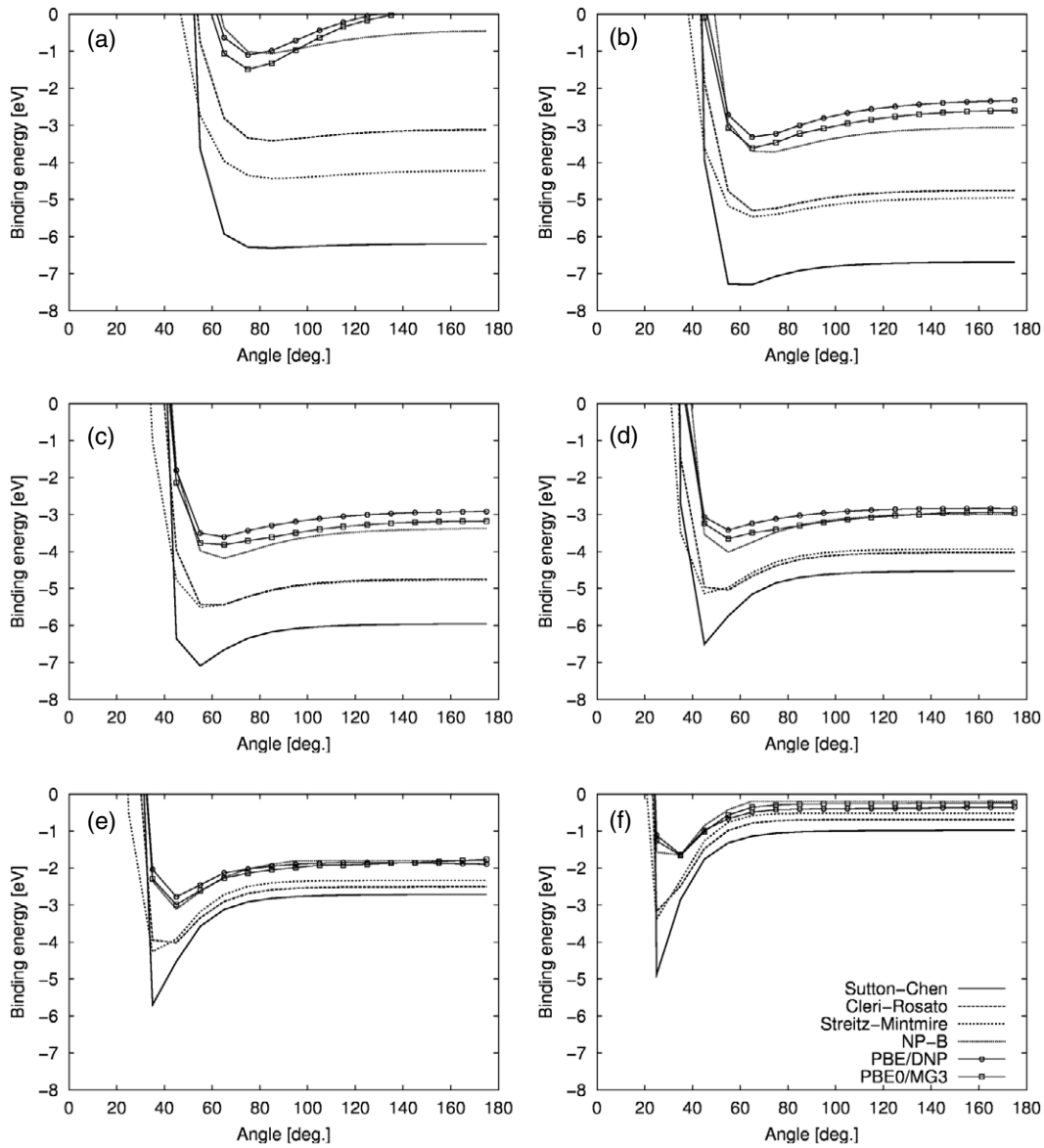


**Figure 3.** Binding energy of Al<sub>3</sub> as a function of angle at different  $r_1, r_2$  separations: (a)  $r_1, r_2 = 2 \text{ \AA}$ , (b)  $r_1, r_2 = 2.3 \text{ \AA}$ , (c)  $r_1, r_2 = 2.506 \text{ \AA}$ , (d)  $r_1, r_2 = 2.863 \text{ \AA}$ , (e)  $r_1, r_2 = 3.5 \text{ \AA}$ , and (f)  $r_1, r_2 = 5 \text{ \AA}$ .

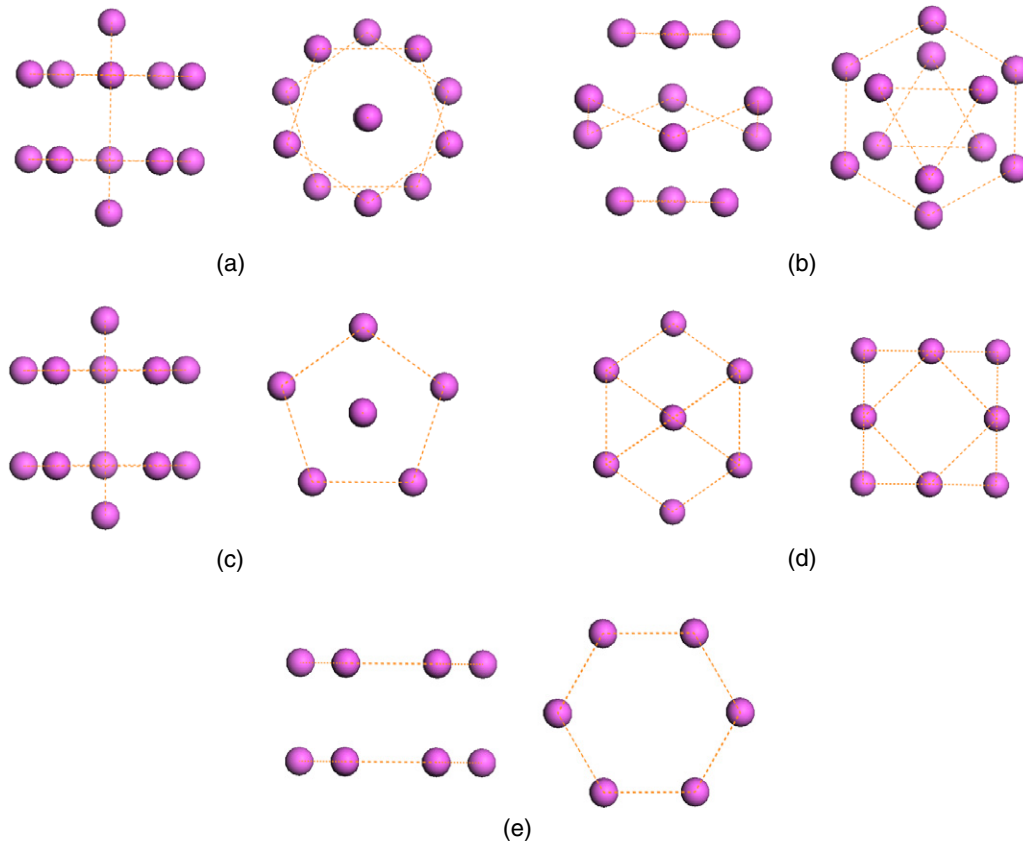


**Figure 4.** Structural isomers of  $\text{Al}_{12}$ , shown from the side (left) and top (right).

**Table 5.** Binding energies (the binding energy for the  $I_h$  symmetry is given as an absolute value, while the rest are given in terms of difference with respect to the  $I_h$  value) for different  $\text{Al}_{12}$  symmetries.

Symmetry	PBE/DNP (eV)	Sutton–Chen (eV)	Cleri–Rosato (eV)	Streitz–Mintmire (eV)	NP-B (eV)
$I_h$	–27.4576 [11]	–32.7915	–29.7736	–29.8411	–27.5103
$D_{3d}$	0.2765	0.0296	0.0579	0.2171	0.0620
$D_{5h}$	0.2781	0.0305	0.0583	0.2175	0.0621
$O_h$	1.1265	0.4680	0.9151	0.9920	1.1510
$D_{6h}$	2.0938	0.6140	1.1430	1.2251	1.4290

### 3.4. $\text{Al}_{12}$ and $\text{Al}_{13}$

In this section, we investigate the performance of the potentials for the determination of the structures and relative energies of isomers of  $\text{Al}_{12}$  and  $\text{Al}_{13}$ . Table 5 presents the binding energies for a selection of structural isomers of  $\text{Al}_{12}$  (figure 4). In all cases, the  $I_h$  symmetric isomer is found to be the lowest in energy. However, as can be seen in table 5, there is quite a range in the calculated binding energies relative to the benchmark PBE/DNP values. Not surprisingly, the NP-B value is in close agreement with the PBE/DNP value. For the bulk-fitted potentials, Cleri–Rosato gives the closest agreement with the PBE/DNP value, closely followed by Streitz–Mintmire, while Sutton–Chen gives the largest error. The binding energies for the remaining isomers are given relative to the values for the structure in  $I_h$  symmetry, which was found to be the lowest energy isomer given by PBE/DNP. It is noteworthy that all of the potentials studied in this work

give the correct ordering of binding energies, including the ordering of the  $I_h$  and  $D_{3d}$  symmetries that are observed to differ by only 0.0015 eV using PBE/DNP. The NP-B potential also predicts that these two isomers are essentially degenerate, with only  $10^{-4}$  eV separating the two isomers. However, the energy difference at all levels, including DFT, between these symmetries is small and substantially less than thermal energy at room temperature. In general, binding energies obtained with the NP-B potential are within 0.13 eV of the PBE/DNP values. In comparison, Cleri–Rosato and Streitz–Mintmire values differ from PBE/DNP on average by 2.7 and 2.8 eV, respectively, while the average error for the Sutton–Chen potential is 6.2 eV.

Table 6 shows the characteristic distances for the  $I_h$  isomer of  $\text{Al}_{12}$  (figure 5) determined using geometry optimization with each of the EAM potentials and compared with the PBE/DNP values [11]. The Sutton–Chen potential significantly underestimates all of the key distances, with an average



**Table 6.** Characteristic distances for the Al<sub>12</sub> cluster with I<sub>h</sub> symmetry.

Distance type	PBE/DNP (Å) [11]	Sutton–Chen (Å)	Cleri–Rosato (Å)	Streitz–Mintmire (Å)	NP-B (Å)
Al <sub>1</sub> –Al <sub>2</sub>	2.724	2.562	2.679	2.665	2.720
Al <sub>l</sub> –CAI	1.432	1.347	1.409	1.401	1.430
CAI–CAI	2.317	2.180	2.279	2.267	2.314
COM–Al <sub>s</sub>	2.591	2.437	2.548	2.535	2.587
Al <sub>l</sub> –Al <sub>l</sub>	5.181	4.874	5.096	5.070	5.174
Average deviation		–5.93%	–1.64%	–2.16%	–0.14%

**Table 7.** Binding energies (the binding energy for the D<sub>3d</sub> symmetry is given as an absolute value, while the rest are given relative to the D<sub>3d</sub> value) for different Al<sub>13</sub> symmetries.

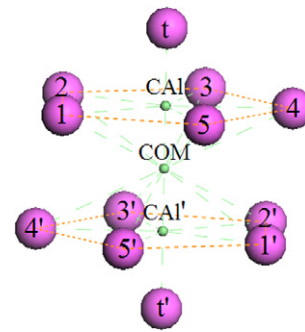
Symmetry	PBE/DNP (eV)	Sutton–Chen (eV)	Cleri–Rosato (eV)	Streitz–Mintmire (eV)	NP-B (eV)
D <sub>3d</sub>	–31.7136	–36.3230	–33.8064	–34.1071	–31.8873
I <sub>h</sub>	0.0027 [11]	0.0044	0.0004	0.0006	–0.0015
D <sub>5h</sub>	0.2962	0.2848	0.6038	0.5836	0.8283
C <sub>s</sub>	0.5649	0.3644	0.7085	0.6917	0.9287
O <sub>h</sub>	1.0940	0.3226	0.7078	0.7035	0.9166
D <sub>6h</sub>	2.7781	0.7995	2.3248	2.2131	3.2739

**Table 8.** Characteristic distances for the Al<sub>13</sub> cluster with I<sub>h</sub> symmetry.

Distance type	PBE/DNP (Å) [11]	Sutton–Chen (Å)	Cleri–Rosato (Å)	Streitz–Mintmire (Å)	NP-B (Å)
Al <sub>1</sub> –Al <sub>2</sub>	2.808	2.694	2.796	2.792	2.841
Al <sub>l</sub> –CAI	1.476	1.417	1.470	1.468	1.494
CAI–CAI	2.388	2.292	2.379	2.375	2.417
COM–Al <sub>s</sub>	2.670	2.563	2.660	2.655	2.702
Al <sub>l</sub> –Al <sub>l</sub>	5.340	5.125	5.319	5.311	5.404
Average deviation		–4.02%	–0.40%	–0.55%	+1.20%

deviation of 5.93% compared to PBE/DNP. Cleri–Rosato and Streitz–Mintmire also tend to slightly underestimate the key distances, but to a lesser extent (1.64% and 2.16%, respectively). This may be due to the overestimation of the binding energy by these potentials, as evidenced from table 5. Again, the NP-B potential, which was fitted to small cluster data, performed extremely well with a deviation of only 0.14% relative to the PBE/DNP results.

As a further test of the potentials, we investigate the structures and relative binding energies of isomers of Al<sub>13</sub> (figure 6). The binding energies of Al<sub>13</sub> isomers are shown in table 7 relative to the values for the structure in D<sub>3d</sub> symmetry; the lowest energy symmetry given by PBE/DNP. All levels considered predict that the D<sub>3d</sub> and I<sub>h</sub> isomers are very close in energy, with D<sub>3d</sub> slightly favoured, except for NP-B, which favours the I<sub>h</sub> isomer. However, despite the minor discrepancy, the NP-B potential gives the closest absolute binding energies for these isomers compared to PBE/DNP. All levels predict that the D<sub>5h</sub> structure is next highest in energy. However, all of the potentials predict a much smaller separation in the binding energies of the C<sub>s</sub> and O<sub>h</sub> isomers compared to PBE/DNP and generally predict O<sub>h</sub> to be slightly lower in energy than C<sub>s</sub>. All levels predict D<sub>6h</sub> to be of significantly higher energy than the other isomers. In terms of absolute binding energies, NP-B performs the best with an average deviation from PBE/DNP of 0.17 eV which is lower than the MUE reported by Jasper *et al* (0.67 eV) [28]. The difference is likely due to the

**Figure 5.** Schematic diagram of an Al<sub>12</sub> cluster, showing the labelling and the centroids used for the structural analysis. For Al<sub>13</sub>, an additional aluminium atom occupies the COM position.

large number of structures in the Al<sub>13</sub> group (consisting of Al<sub>9</sub> to Al<sub>13</sub>) in Jasper *et al*'s data set [28]. Sutton–Chen differs by an average of 1.3 eV, while the Cleri–Rosato and Streitz–Mintmire potentials differ by an average of 0.41 and 0.49 eV, respectively. Jasper *et al* reported the MUEs from PBE0/MG3 to be 2.38, 3.26, and 1.27 eV, respectively for the Al<sub>13</sub> data set [48]. The deviations between the EAM methods and PBE/DNP for Al<sub>13</sub> cluster are generally lower than those for Al<sub>12</sub> cluster.

Table 8 shows the characteristic distances of the I<sub>h</sub> isomer of Al<sub>13</sub> obtained by geometry optimization with the

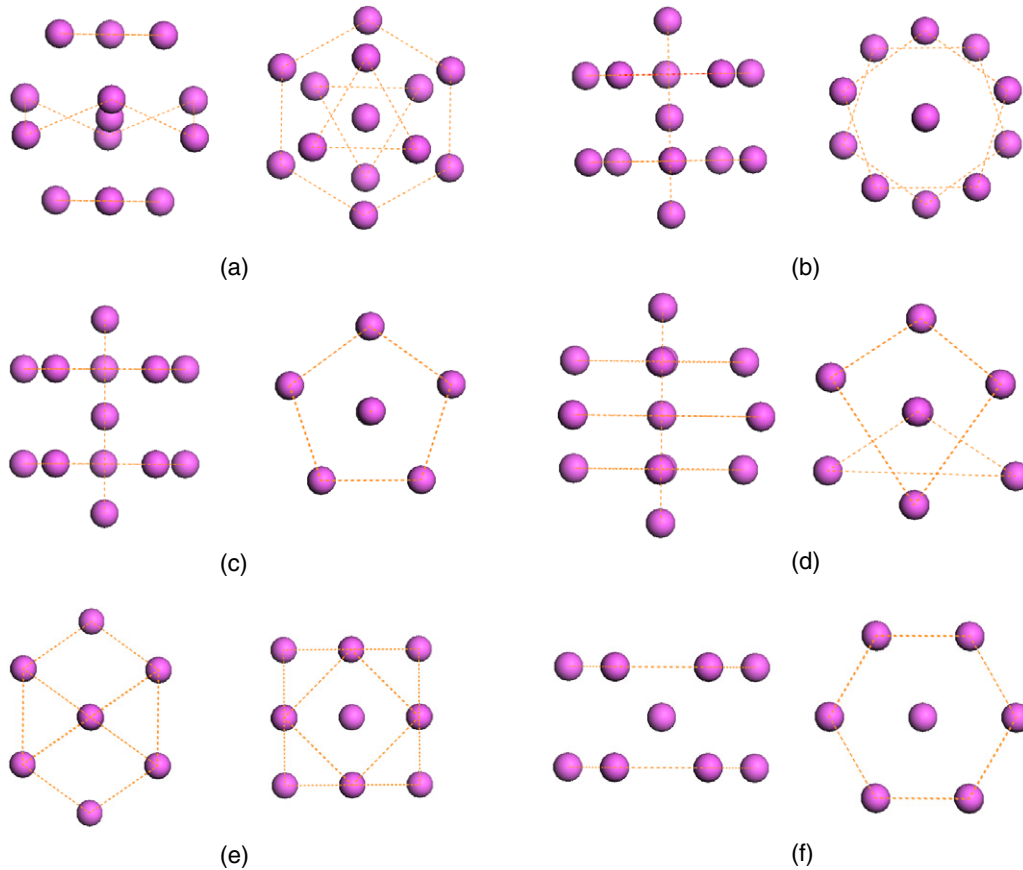


**Figure 6.** Structural isomers of  $Al_{13}$ , shown from the side (left) and top (right).

different potentials. Similar to the results for  $Al_{12}$  clusters, the Sutton–Chen potential underestimates the key distances, with an average deviation of 4.02% from PBE/DNP, which is also reflected in the overestimation of the binding energy as shown in table 5. The NP-B potential only slightly overestimates the distances, with an average deviation of 1.20%. Surprisingly, the Cleri–Rosato and Streitz–Mintmire potentials performed extremely well for the structure of  $Al_{13}$ , with average deviations of 0.40% and 0.55%, respectively.

### 3.5. $Al_{34}$ and $Al_{55}$

After evaluating the performance of the EAM potentials on small clusters, we provide a preliminary examination of the melting process for two larger clusters ( $Al_{34}$  and  $Al_{55}$ ), determined using each of the potentials. The potentials are compared in terms of the characteristic nearest neighbour distances of the clusters, Lindemann index, which can be used to measure the melting process [51–53], and melting temperature. The Lindemann index is a measure of the relative root-mean-square bond-length fluctuation and is defined as

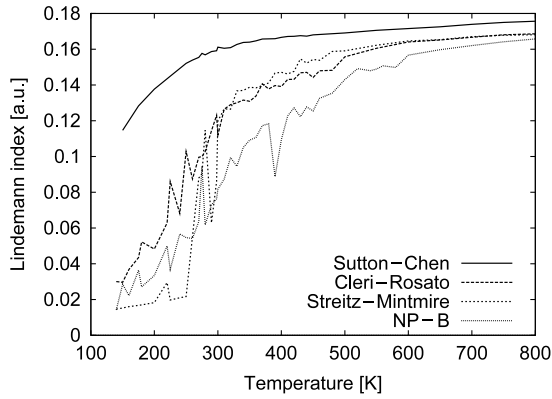
$$\delta = \frac{2}{N(N-1)} \sum_{i < j} \frac{\sqrt{\langle r_{ij}^2 \rangle_t - \langle r_{ij} \rangle_t^2}}{\langle r_{ij} \rangle_t},$$

where  $r_{ij}$  is the separation between atoms  $i$  and  $j$ ,  $N$  is the number of atoms, and the  $\langle \rangle_t$  symbols indicate time average.

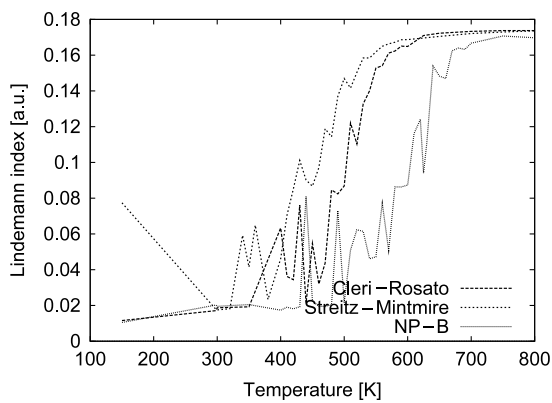
At temperatures below the melting point, the individual atoms of the cluster vibrate around their equilibrium positions. However, the bond length between any two atoms will not change significantly from their equilibrium values. As the temperature is increased beyond the melting point, the atoms gain translational freedom and deviate from their equilibrium positions, thus increasing the Lindemann index significantly.

Figure 7 presents the Lindemann index as a function of temperature for  $Al_{34}$ . All the potentials exhibit a straightforward, one-stage melting process. However, the  $Al_{34}$  cluster modelled with the Sutton–Chen potential is predicted to melt at a temperature below 200 K, which is outside the range of temperatures considered in this study. Puri and Yang also confirmed the Sutton–Chen potential to severely underestimate the melting temperature of bulk and large aluminium clusters (up to 9 nm in diameter) [54]. However, the Cleri–Rosato, Streitz–Mintmire, and NP-B potentials all give similar performance, with the Lindemann indices that start at  $\sim 0.02$  at 150 K and increase to  $\sim 0.16$  at 800 K after melting.

Table 9 presents the melting temperatures of the cluster determined from the Lindemann index as predicted by the potentials. In this work, we have defined the melting temperature as the point where the Lindemann index is halfway between the two boundary values. The melting temperature of the Sutton–Chen potential cannot be calculated from the data that we obtained for this study. All the other potentials predict melting temperatures that are relatively consistent (with



**Figure 7.** Lindemann index of the  $\text{Al}_{34}$  cluster as a function of temperature for the EAM potentials.



**Figure 8.** Lindemann index of the  $\text{Al}_{55}$  cluster as a function of temperature for the EAM potentials.

**Table 9.** Melting temperatures of  $\text{Al}_{34}$  cluster.

EAM potential	$T_m$ (K)
Sutton-Chen	<200
Cleri-Rosato	280
Streitz-Mintmire	305
NP-B	350

an average value of 312 K), with  $\sim 70$  K separating the three values. The Cleri-Rosato value is at the lower end of the range (280 K), while NP-B predicts a higher temperature of 350 K.

Figure 8 shows the Lindemann index as a function of temperature for the  $\text{Al}_{55}$  cluster. We have not included the Sutton-Chen results due to the underestimation of the melting temperature observed in  $\text{Al}_{34}$ . As for the  $\text{Al}_{34}$  cluster, the Lindemann indices for the other potentials show a one-stage melting process, with values again starting at  $\sim 0.02$  and increasing to  $\sim 0.16$  after melting.

Table 10 shows the melting temperatures of the  $\text{Al}_{55}$  cluster as predicted by the potentials. The spread of the melting temperatures is larger ( $\sim 100$  K) compared to the  $\text{Al}_{34}$  cluster. The lowest melting temperature was predicted by the Streitz-Mintmire potential at 485 K, which compares favourably with the value found by Alavi and Thompson using the same potential ( $450 \pm 90$  K) [51]. The melting temperature predicted

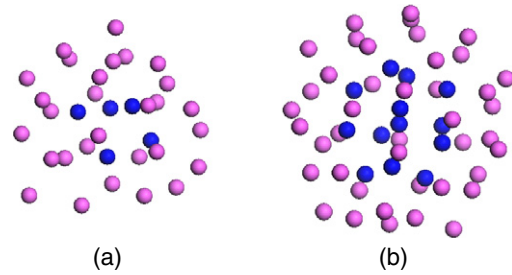


**Figure 9.** The core (blue, or black in the print version) and shell (pink, or grey in the print version) regions of the (a)  $\text{Al}_{34}$  and (b)  $\text{Al}_{55}$  clusters.

**Table 10.** Melting temperatures of  $\text{Al}_{55}$  cluster.

EAM potential	$T_m$ (K)
Cleri-Rosato	515
Streitz-Mintmire	485
NP-B	$450 \pm 90$ [51]
NP-B	585

by the Cleri-Rosato potential is 30 K higher than the Streitz-Mintmire value, while NP-B again predicts a higher melting temperature of 585 K.

In order to evaluate the structural properties of the clusters after melting, two regions have been defined and shown in figure 9 that we will subsequently refer to as the core and shell. Radial distribution functions of the clusters at 800 K (i.e. above the melting temperature) were then obtained on these two regions and the characteristic nearest neighbour distances compared.

Table 11 shows the nearest neighbour distances for the structures obtained with the different potentials. In general, the shell region has a longer nearest neighbour distance compared to the core region. For the  $\text{Al}_{34}$  cluster, Sutton-Chen gives a very short shell nearest neighbour distance, which is related to the underestimation of bond lengths, discussed earlier for smaller clusters that have higher surface atom-to-bulk ratios. Cleri-Rosato and Streitz-Mintmire give no appreciable difference between the core and shell nearest neighbour distances, while NP-B shows a longer shell than core nearest neighbour distance. For the  $\text{Al}_{55}$  cluster, all the potentials give slight variations in the distances, with Cleri-Rosato predicting slightly shorter shell nearest neighbour distances, but well within the margin of uncertainty in the calculation. Overall, the distances are consistent with the analysis on the  $\text{Al}_{12}$  and  $\text{Al}_{13}$  surface atoms discussed in section 3.4, with the NP-B giving the longest nearest neighbour distance between the surface atoms, compared to the other potentials.

#### 4. Conclusions

In this paper, we have compared the performance of three bulk-fitted and a cluster-fitted EAM potential for the determination of the structural and energetic properties of a range of Al clusters, compared to PBE/DNP calculations as a benchmark.

All of the bulk-fitted potentials were observed to overestimate the binding energies for small clusters, with

**Table 11.** Nearest neighbour distances (Å) of the core and shell regions of the Al<sub>34</sub> and Al<sub>55</sub> clusters at 800 K.

Potential	Al <sub>34</sub>		Al <sub>55</sub>	
	Core	Shell	Core	Shell
Sutton–Chen	2.74 ± 0.02	2.59 ± 0.02	—	—
Cleri–Rosato	2.75 ± 0.02	2.75 ± 0.02	2.80 ± 0.02	2.77 ± 0.02
Streitz–Mintmire	2.72 ± 0.02	2.75 ± 0.02	2.76 ± 0.02	2.77 ± 0.02
NP-B	2.74 ± 0.02	2.81 ± 0.02	2.80 ± 0.02	2.83 ± 0.02

largest variations for Al<sub>2</sub> and Al<sub>3</sub>. The Sutton–Chen potential is found unsuitable in predicting the structural properties of these clusters, overestimating the strength of the interactions between aluminium atoms, which results in a 4% underestimation of bond lengths. This may be due to the Sutton–Chen being fitted to just structural data, which does not take into account the energetics data such as the vacancy formation energy and surface energies. The Cleri–Rosato and Streitz–Mintmire potentials were shown to perform rather well for predicting Al<sub>12</sub> and Al<sub>13</sub> structures, although with higher absolute binding energy value differences compared to PBE/DNP results. For the Al<sub>34</sub> and Al<sub>55</sub> clusters, these potentials predict nearest neighbour distances that are slightly shorter compared to the values obtained using the NP-B potential. The melting temperatures predicted by these potentials are also lower compared to the value predicted by the NP-B potential. While this suggests that they can be used to predict the structures of relatively large aluminium clusters reasonably well, the potentials may not be appropriate to predict their energetics.

As expected, the NP-B potential is well suited to studying small aluminium clusters due to its ability to predict both structures and energetics accurately, with results that are very close to those obtained using DFT calculations. However, this potential may not be suitable for use in certain bulk and surface systems due to its inability to predict the elastic properties accurately.

## Acknowledgments

The authors wish to acknowledge the CSIRO Flagship for Hydrogen Materials Alliance for providing funding for this project. JDG would also like to thank the Government of Western Australia for support. We also acknowledge APAC for the grant of computer simulation time.

## References

- [1] Schuth F, Bogdanovic B and Felderhoff M 2004 Light metal hydrides and complex hydrides for hydrogen storage *Chem. Commun.* **20** 2249–58
- [2] Dornheim M, Doppiu S, Barkhordarian G, Boesenberg U, Klassen T, Gutfleisch O and Bormann R 2007 Hydrogen storage in magnesium-based hydrides and hydride composites *Scr. Mater.* **56** 841–6
- [3] Kang J K, Lee J Y, Muller R P and Goddard W A III 2004 Hydrogen storage in LiAlH<sub>4</sub>: predictions of the crystal structures and reaction mechanisms of intermediate phases from quantum mechanics *J. Chem. Phys.* **121** 10623–33
- [4] Zaluska A, Zaluski L and Strom-Olsen J O 2001 Structure, catalysis and atomic reactions on the nano-scale: a systematic approach to metal hydrides for hydrogen storage *Appl. Phys. A* **72** 157–65
- [5] Zidan R A, Takara S, Hee A G and Jensen C M 1999 Hydrogen cycling behavior of zirconium and titanium–zirconium-doped sodium aluminum hydride *J. Alloys Compounds* **285** 119–22
- [6] Ahlrichs R and Elliott S D 1999 Clusters of aluminium, a density functional study *Phys. Chem. Chem. Phys.* **1** 13–21
- [7] Henry D J, Varano A and Yarovsky I 2008 An assessment on the performance of DFT with numerical basis set to describe small aluminium cluster *J. Phys. Chem. A* **112** 9835–44
- [8] Delley B 1990 An all-electron numerical-method for solving the local density functional for polyatomic-molecules *J. Chem. Phys.* **92** 508–17
- [9] Delley B 2000 From molecules to solids with the DMol(3) approach *J. Chem. Phys.* **113** 7756–64
- [10] Yarovsky I and Goldberg A 2005 DFT study of hydrogen adsorption on Al-13 clusters *Mol. Simul.* **31** 475–81
- [11] Goldberg A and Yarovsky I 2007 Density functional theory study of hydrogen adsorption on Al<sub>12</sub> cages *Phys. Rev. B* **75** 195403
- [12] Henry D J, Varano A and Yarovsky I 2008 H<sub>2</sub> dissociates spontaneously between Al<sub>12</sub>Mg clusters, in preparation
- [13] Bogdanovic B, Eberle U, Felderhoff M and Schuth F 2007 Complex aluminum hydrides *Scr. Mater.* **56** 813–6
- [14] Zaluska A, Zaluski L and Strom-Olsen J O 2000 Sodium alanates for reversible hydrogen storage *J. Alloys Compounds* **298** 125–34
- [15] Balde C P, Hereijgers B P C, Bitter J H and de Jong K P 2008 Sodium alanate nanoparticles—linking size to hydrogen storage properties *J. Am. Chem. Soc.* **130** 6761–55
- [16] Basic Energy Sciences (BES) Advisory Committee 2003 *Basic Research Needs for the Hydrogen Economy: Report of the Basic Energy Sciences Workshop on Hydrogen Production, Storage, and Use*
- [17] Daw M S and Baskes M I 1983 Semiempirical, quantum mechanical calculation of hydrogen embrittlement in metals *Phys. Rev. Lett.* **50** 1285–988
- [18] Daw M S, Foiles S M and Baskes M I 1993 The embedded-atom method: a review of theory and applications *Mater. Sci. Rep.* **9** 251–310
- [19] Baskes M I 1992 Modified embedded-atom potentials for cubic materials and impurities *Phys. Rev. B* **46** 2727–42
- [20] Cherne F J, Baskes M I and Deymier P A 2001 Properties of liquid nickel: a critical comparison of EAM and MEAM calculations *Phys. Rev. B* **65** 024209
- [21] Jelinek B, Houze J, Kim S, Horstemeyer M F, Baskes M I and Kim S-G 2007 Modified embedded-atom method interatomic potentials for the Mg–Al alloy system *Phys. Rev. B* **75** 054106
- [22] Baskes M I, Angelo J E and Moody N R 1996 *Hydrogen Effects in Materials* ed A W Thompson and N R Moody (Warrendale, PA: The Minerals, Metals and Materials Society) pp 77–89
- [23] Cleri F and Rosato V 1993 Tight-binding potentials for transition metals and alloys *Phys. Rev. B* **48** 22–33

- [24] Streitz F H and Mintmire J W 1994 Electrostatic potentials for metal-oxide surfaces and interfaces *Phys. Rev. B* **50** 11996–2003
- [25] Sutton A P and Chen J 1990 Long-range Finnis–Sinclair potentials *Phil. Mag. Lett.* **61** 139–46
- [26] Tanguy D and Magnin T 2003 Atomic-scale simulation of intergranular segregation of H in Al–Mg: implications for H-induced damage *Phil. Mag.* **83** 2995–4009
- [27] Mei J and Davenport J W 1992 Free-energy calculations and the melting point of Al *Phys. Rev. B* **46** 21–5
- [28] Jasper A W, Schultz N E and Truhlar D G 2005 Analytic potential energy functions for simulating aluminum nanoparticles *J. Phys. Chem. B* **109** 3915–20
- [29] Li Z H, Bhatt D, Schultz N E, Siepmann J I and Truhlar D G 2007 Free energies of formation of metal clusters and nanoparticles from molecular simulations:  $Al_n$  with  $n = 2–60$  *J. Phys. Chem. C* **111** 16227–42
- [30] Mei J, Davenport J W and Fernando G W 1991 Analytic embedded-atom potentials for fcc metals: application to liquid and solid copper *Phys. Rev. B* **43** 4653–8
- [31] Gale J D 1997 GULP: a computer program for the symmetry-adapted simulation of solids *J. Chem. Soc. Faraday Trans.* **93** 629–37
- [32] Shanno D F 1970 Conditioning of quasi-Newton methods for function minimization *Math. Comput.* **24** 647–56
- [33] Banerjee A, Adams N, Simons J and Shepard R 1985 Search for stationary-points on surface *J. Phys. Chem.* **89** 52–7
- [34] Perdew J P, Burke K and Ernzerhof M 1996 Generalized gradient approximation made simple *Phys. Rev. Lett.* **77** 3865–8
- [35] Perdew J P, Burke K and Ernzerhof M 1997 Generalized gradient approximation made simple *Phys. Rev. Lett.* **78** 1396
- [36] Fowler J E and Ugalde J M 1998 Al-12 and the Al@Al-12 clusters *Phys. Rev. A* **58** 383–8
- [37] Kittel C 1971 *Introduction to Solid State Physics* (New York: Wiley)
- [38] Kittel C 1966 *Introduction to Solid State Physics* (New York: Wiley)
- [39] Kittel C 1976 *Introduction to Solid State Physics* (New York: Wiley)
- [40] Gaudoin R, Foulkes W M C and Rajagopal G 2002 *Ab initio* calculations of the cohesive energy and the bulk modulus of aluminium *J. Phys.: Condens. Matter* **14** 8787–93
- [41] Ashcroft N W and Mermin N D 1976 *Solid State Physics* (Philadelphia, PA: Saunders)
- [42] Gaudoin R and Foulkes W M C 2002 *Ab initio* calculations of bulk moduli and comparison with experiment *Phys. Rev. B* **66** 052104
- [43] Lide D R (ed) 2005 *CRC Handbook of Chemistry and Physics* vol 85 (Boca Raton, FL: CRC Press)
- [44] Hirth J P and Lothe J (ed) 1982 *Theory of Dislocation* (New York: Wiley)
- [45] Simmons G and Wang H (ed) 1971 *Single Crystal Elastic Constants and Calculated Aggregated Properties* (Cambridge, MA: MIT Press)
- [46] James A M and Lord M P 1992 *Macmillan's Chemical and Physical Data* (London: Macmillan)
- [47] Ho P S and Ruoff A L 1969 Pressure dependence of the elastic constants for aluminum from 77 to 300 K *J. Appl. Phys.* **40** 3151–6
- [48] Jasper A W, Staszewski P, Staszewska G, Schultz N E and Truhlar D G 2004 Analytic potential energy functions for aluminum clusters *J. Phys. Chem. B* **108** 8996–9010
- [49] Schultz N E, Staszewska G, Staszewski P and Truhlar D G 2004 Validation of theoretical methods for the structure and energy of aluminum clusters *J. Phys. Chem. B* **108** 4850–61
- [50] Langhoff S R and Bauschlicher J C W 1990 Theoretical study of the spectroscopy of  $Al_2$  *J. Chem. Phys.* **92** 1879–86
- [51] Alavi S and Thompson D L 2006 Molecular dynamics simulations of the melting of aluminium nanoparticles *J. Phys. Chem. A* **110** 1518–23
- [52] Lee J Y, Maeng J Y, Lee E-K, Kim B, Kim S and Han K-K 2000 Melting behaviors of icosahedral metal clusters studied by Monte Carlo simulations *J. Comput. Chem.* **21** 380–7
- [53] Zhou Y, Karplus M, Ball K D and Berry R S 2002 The distance fluctuation criterion for melting: comparison of square-well and Morse potential models for clusters and homopolymers *J. Chem. Phys.* **116** 2323–9
- [54] Puri P and Yang V 2007 Effect of particle size on melting of aluminum at nano scales *J. Phys. Chem. C* **111** 11776–83